PHYSICAL REVIEW B **105**, 235422 (2022)

Magnetic proximity induced valley-contrasting quantum anomalous Hall effect in a graphene-$CrBr_3$ van der Waals heterostructure

Mayuri Bora,[1] Sushant Kumar Behera,[2,3] Prasanjit Samal,[2] and Pritam Deb[1,*]

[1]*Department of Physics, Tezpur University (Central University), Tezpur-784028, India*
[2]*School of Physical Sciences, National Institute of Science Education and Research, HBNI, Bhubaneswar-752050, India*
[3]*Materials Research Centre, Indian Institute of Science, Bangalore-560012, India*

(Received 1 February 2022; revised 6 May 2022; accepted 1 June 2022; published 13 June 2022)

The magnetic proximity effect is an imperative tool to comprehend the valley contrasting quantum anomalous Hall (QAH) effect in van der Waals (vdW) heterostructure. The introduction of magnetic exchange and spin orbit interaction together enables to realize topological phases, with a particular emphasis on an interface can be envisioned towards dissipationless electronics. Herein, the proximity coupled valley contrasting QAH effect is predicted in vdW heterostructure consisting of graphene and a ferromagnetic (FM) semiconductor $CrBr_3$ with the implication of relativistic effect, from the *ab initio* density functional theory (DFT) simulation. The valley contrasting QAH effect is observed with a nonzero Chern number at a high-symmetry point stemming from Berry curvature and Wannier charge center (WCC), leading to a topologically nontrivial state. The occurrence of strong magnetic proximity coupling between graphene and $CrBr_3$ monolayer is realized intrinsically, from shifting of Hall coefficient value near Fermi level. The opening of the global band gap (178 meV) is observed with the inclusion of spin orbit coupling (SOC). The anomalous Hall conductivity (AHC) demonstrates the presence of two maxima peaked at valley K' and K. The observation of AHC is mainly dominated by nonzero surface charge and localized potential at the heterointerface due to proximity interaction. The Fermi level is found to be located exactly inside the nontrivial global band gap, which can be tuned effectively by applying the external electric field or by introducing a staggered sublattice potential. This robustness makes experimental fabrication highly favorable for developing a valley contrasting QAH device prototype.

DOI: 10.1103/PhysRevB.105.235422

I. INTRODUCTION

Magnetic proximity effect (MPE) [1] in two-dimensional (2D) vdW crystals exploit astonishing opportunities in manipulating the electronic and nontrivial topological effects of neighboring material. Magnetic ordering via MPE and spin-orbit coupling (SOC) breaks time reversal symmetry (TRS) and opens a nontrivial global band gap near Dirac states, which induces nontrivial topological phases elucidated by the Chern number at zero external magnetic field [2,3]. The quantum anomalous hall effect (QAHE) is one of such fascinating physical phenomena [4–6], creating dissipationless chiral nature of edge transport phenomena and manifesting Hall conductance $\sigma_{xy} = e^2/h$, which holds a potential platform for low-power spintronic devices [7,8]. Moreover, breaking of inversion symmetry in a 2D honeycomb lattice has unequal carriers and the binary degrees of freedom peaked at valleys K' and K, resulting in valley contrasting QAH effect [9]. The nonzero values of valleys are well preserved in Brillouin zone with no interaction among the valleys. Because of the presence of localized valley, the Hall conductivity becomes nonzero, resulting in quantum valley Hall (QVH) effect [10,11]. The valley contrasting QAHE has been theoretically predicted through the external addition of a bilayer nonmagnetic system, superlattices, vacancies, or antiferromagnetic (AFM) substrates on a nonmagnetic system having limitations in maintaining magnetic ordering [4,12–15]. The coexistence of Ising and Rashba SOC in TMD gives rise to the valley Hall effect. Near the conduction band edge, the valley contrasting Berry curvature can be tuned by gating and intrinsically by orbital degrees of freedom obtaining magnetic textures [16,17]. The coexistence of a long-range magnetic order along with relativistic effect [18] is the most crucial and challenging tasks to experimentally realize anomalous behavior. In this regard, MPE depicts an effective approach to overcome the limitation by coupling long-range magnetic order induced by ferromagnetic (FM) or AFM vdW crystal along with SOC for realizing valley contrasting QAH effect [19]. Therefore designing of a robust valley localized QAH vdW crystal is of a significant interest in nurturing further progress in this area.

Graphene is an appropriate model system for predicting topologically nontrivial phases because of its unique honeycomb lattice exhibiting high electron densities and long spin-relaxation lengths [20]. However, pristine graphene is nonmagnetic in nature and has very weak intrinsic SOC of about 12 μeV with a very small nontrivial band gap [21]. The coexistence of ferromagnetism and SOC in a material predicts valley contrasting QAHE [22]. Moreover, long-range magnetic ordering in topological insulators (TI) can be induced due to the proximity coupling with a ferromagnetic insulator (FI) [23,24]. As compared to the thickness of a few quintuple

---

[*] Corresponding author: pdeb@tezu.ernet.in (Pritam Deb).

layers of surface states of TI, a single atomic layer of graphene gives much stronger hybridization when coupled with a substrate. In this regard, the proximity effect in graphene should be technically higher than that in TI. Recently, 2D magnetism has gained the significant attention due to its intrinsic long-range magnetic order in atomically layered crystals [25] for realizing an anomalous and topologically nontrivial state. In addition to SOC and magnetism, possible tuning of a band gap by applying a perpendicular electric field can extend an additional projection to engineer nontrivial topological phases [26,27]. In this regard, the proximity effect has been realized in bilayer graphene (BLG) for manipulating the electronic structure by layer localization of low energy states [26]. Also, $3d$-$5d$ interfaces can be modulated by altering the Rashba spin-orbit interaction with the application of external electric field [28]. Therefore such external perturbations can harness both SOC and magnetism by configuring the wave function localization induced exchange splitting in the electronic structure. This entails new opportunities by introducing 2D magnets with graphene coupled via proximity effect, SOC and external electric field in view of designing vdW heterostructure to generate quantum valley Hall (QVH) effect.

In this study, we have considered heterostructure combining semimetal graphene and a 2D ferromagnet, $\mathrm{CrBr_3}$ [29–31] for realization of QVH effect in graphene. $\mathrm{CrBr_3}$ is a 2D ferromagnet with Curie temperature of about ∼33 K [32] and it can possibly induce strong SOC in graphene through hybridization via proximity coupling [10,31]. $\mathrm{CrBr_3}$ exhibits hexagonal crystal structure, which matches well with that of graphene. We explore the possibility of inducing time reversal symmetry (TRS) and inversion symmetry breaking following the previous work [33]. A robust valley localized QAH effect is realized in Gr-$\mathrm{CrBr_3}$ vdW heterostructure based on *ab initio* DFT calculations and WANNIER90 tools. By analyzing Berry curvature, Wannier charge center (WCC) and anomalous Hall conductivity (AHC) we found an odd winding number ($C_v = 1$) indicating heterostructure system to be topologically nontrivial and gives rise to QVH effect. The Fermi (E_F) energy is located exactly inside a nontrivial global band gap, favorable for designing dissipationless low-power electronic devices.

II. COMPUTATIONAL DETAILS

The ground state energy optimization and electronic structure calculations were performed by using *ab initio* methods based on density functional theory (DFT), as implemented in QUANTUM ESPRESSO (QE) [34] codes. The Perdew-Burke-Ernzerhof (PBE) generalized gradient approximation (GGA) is employed to describe exchange and correlation functional [35]. To describe Cr $3d$ electrons, GGA+U method is adopted [36] and the values of on-site Coulomb interaction U and exchange interaction J are set to be 3.0 and 0.9 eV, respectively. The plane wave cut off energy is set to 500 eV and a vacuum space of 22 Å is used to avoid interactions between two adjacent layers. The 6 × 6 × 1 and 27 × 27 × 1 Monkhorst-Pack grids are adopted for Gr-$\mathrm{CrBr_3}$ heterostructure, respectively, to conduct first Brillouin zone integration. For vdW heterostructures, more accurate and expensive hybrid functional HSE06 [37] is adopted to achieve the optimized geometry structures and electronic state calculations including local potential distribution as implemented in the Vienna *ab initio* simulation package (VASP) [38]. The vdW correction with Grimme (DFT-D2) method [39] is considered in heterostructure calculation. For calculations of topological properties, maximally localized Wannier functions (MLWFs), Berry curvatures, anomalous Hall conductivity are constructed by employing the WANNIER90 package [40]. WANNIERTOOL [41] is used for calculating the evolution of Wannier charge center (WCC).

III. RESULTS AND DISCUSSIONS

The crystal geometry and corresponding interplanar spacing notations were achieved by utilizing ground state optimization using Feynman-Hellman theorem. The Gr-$\mathrm{CrBr_3}$ vdW heterostructure system has obtained ground state energy configuration when ferromagnetic ordering and relativistic effect is considered for robust theoretical calculation. The stable crystal geometries with different views having the interplanar spacing of 0.13 Å between graphene and monolayer $\mathrm{CrBr_3}$ is shown in Figs. 1(a)–1(c). Therefore, at an interplanar spacing of 0.13 Å, two monolayers will hybridize effectively to induce proximity coupling along with SOC. The dispersion correction is considered for optimization of interplanar spacing for close proximity interaction between graphene and $\mathrm{CrBr_3}$. The interplanar spacing is contemplated as a vdW type. As shown in Fig. 1(b), the unit cell consists of two Cr atoms, where one situates at void site named as A and other one situates at top site named as B. Since both A and B belong to disparate sublattices of graphene, such heterointerfaces help in inducing staggered sublattice potential, which commend valley contrasting Hall effect in graphene [42] and designate to QVH phases. Figure 1(d) displays band topology of Gr-$\mathrm{CrBr_3}$ heterostructure along high-symmetry points of first Brillouin zone in our DFT calculations with consideration of relativistic effect. When graphene is located above $\mathrm{CrBr_3}$, it becomes magnetically active due to proximity coupling between C p and Cr d orbitals, which relatively makes heterostructure magnetic in nature. As shown in Fig. 2(a), the heterostructure without consideration of SOC is a gapless system, which can be assigned to degeneracy of C spin-down p orbitals at K point. The system is spin-polarized and topologically protected by C_1 symmetry of heterostructure system. When SOC is considered in Fig. 1(d), a large global band gap of 178 meV is opened near the Fermi level. In the zoomed-in image of the electronic band structure at M-K-Γ, band folding is observed near the Fermi level, which utters the signature of topology in the heterostructure system. The band folding like a W shape at the Fermi level is observed due to the presence of SOC, staggered sublattice potential, and proximity interaction in a heterolayer system. The opening of a global band gap is mainly responsible due to SOC leading to the splitting of the energy levels having different orbitals and the hybridization occurs among the orbitals due to proximity integration as shown in Fig. 2(c). The TRS breaking is due to strong hybridization when graphene is coupled in close proximity with magnetic $\mathrm{CrBr_3}$ and inversion symmetry is broken due to presence of uneven surface charge distribution in heterostructure system. In this regard, the consideration of SOC is important for the splitting of the energy level along

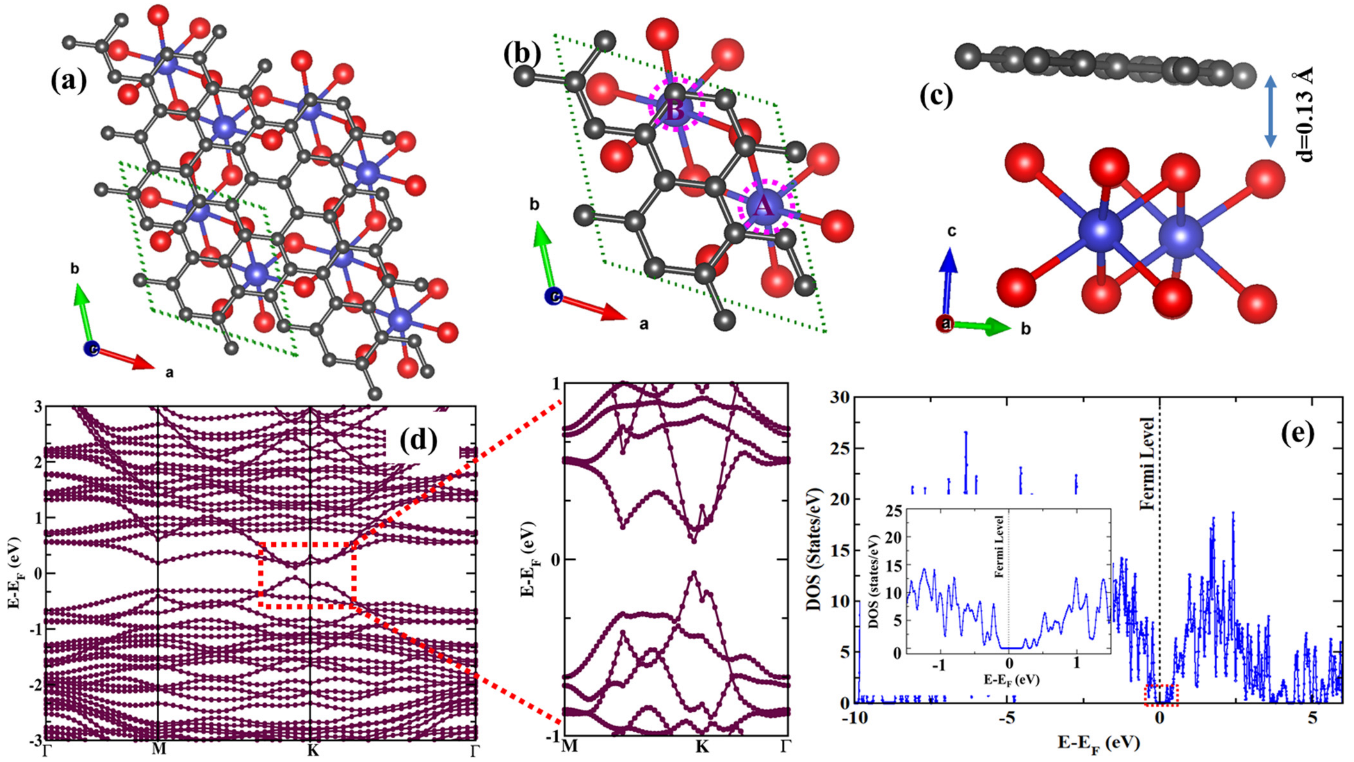

FIG. 1. Crystal structure of Gr-CrBr$_3$ heterostructure. (a) Top view of atomic structure of Gr-CrBr$_3$ heterostructure in supercell 2 × 2 × 1. (b) Top view of atomic structure of Gr-CrBr$_3$ heterostructure in unit cell. (c) Side view of Gr-CrBr$_3$ unit cell with interplanar spacing notation of $d = 0.13$ Å. The grey, blue, and red balls describe carbon (C), chromium (Cr), and bromine (Br), respectively. (d) Electronic band structure of Gr-CrBr$_3$ van der Waals heterostructure in presence of SOC. Zoomed-in picture shows band topology near Fermi level. (e) Density of states (DOS) calculation for Gr-CrBr$_3$ heterostructure in presence of SOC. Zoomed-in inset shows the flat states near Fermi level.

with the opening of the global band gap by lifting the degeneracy, which speculates the possibility of valley contrasting anomalous behavior as shown in a zoomed image of Fig. 2(b). Figure 1(e) shows the density of states (DOS) calculation for Gr-CrBr$_3$ heterolayer system. We observe flat states near the Fermi level indicating the opening of a gap with the implication of the relativistic effect, which corroborates with band topology of a heterolayer system. The spike nature in the DOS pattern speculates the presence of magnetic behavior in the heterobilayer system due to magnetic proximity coupling. Therefore the combined effect will trigger topological phases in a Gr-CrBr$_3$ heterostructure system.

Figure 2(a) displays the position of Dirac cone near Fermi energy region, which strongly dependent on the interlayer separation of $d = 0.13$ Å without implementation of SOC. The Dirac cone is topologically protected near the Fermi level as shown in the inset of Fig. 2(a). The cyan and blue colors denote spin-down and spin-up states manifests electronic character of both graphene and CrBr$_3$ due to the presence of magnetic proximity coupling. Figure 2(b) displays the projected band of the Gr-CrBr$_3$ heterostructure with implications of the relativistic effect. The direct band gap opening is observed near the Fermi region at high-symmetry points K and K' owing to the semiconducting nature of Gr-CrBr$_3$ heterostructure systems supported with electronic band structures shown in Fig. 1(d). Moreover, the conduction band minimum (CBM) and valence band maximum (VBM) near Fermi energy at K point are mainly dominated by antibonding bromine (Br) p_z orbitals, bonding between carbon (C) $p_y + p_z$ orbitals, and chromium (Cr) $d_x^2 - y^2 + d_{xy}$ orbitals denoted by blue, green, and yellow colors, respectively. Due to the presence of proximity coupling between graphene and CrBr$_3$, a strong hybridization occurs among C p and Cr d orbitals and splitting of these orbitals into different energy levels with inclusion of SOC. From overlapping states near the Fermi level as shown in Fig. 2(a) to transition of gap opening in Fig. 2(b) resembles hybridization via proximity effect between $p_y + p_z$ orbitals of C atoms and $d_x^2 - y^2 + d_{xy}$ orbitals of Cr atoms. The opening of the global band gap near K point corresponds to single topological phase transition. This topological phase transition occurs at valley K, which is mainly responsible for staggered AB sublattice potential exist due to close proximity integration. The zoomed image of Fig. 2(b) shows the splitting of the energy level and opening of the global band gap at the high-symmetry point, which correlates well with Fig. 1(d) implementing SOC effect. Figure 2(c) depicts projected DOS of Gr-CrBr$_3$ heterostructure in presence of SOC. Figure 2(c) correlates well with the DOS pattern in Fig. 1(e) and projected bands in Figure 2(a) with less dense orbital states near the Fermi level with a distinct difference between conduction and valence bands leading to the opening of a gap due to the existence of relativistic effect. The total orbital contribution of Gr-CrBr$_3$ heterostructure systems is observed where the conduction band region is mainly dominated by Cr d and C p orbitals. The hybridization among C p and Cr d orbitals is clearly evident from the dynamic behavior of atomic orbitals

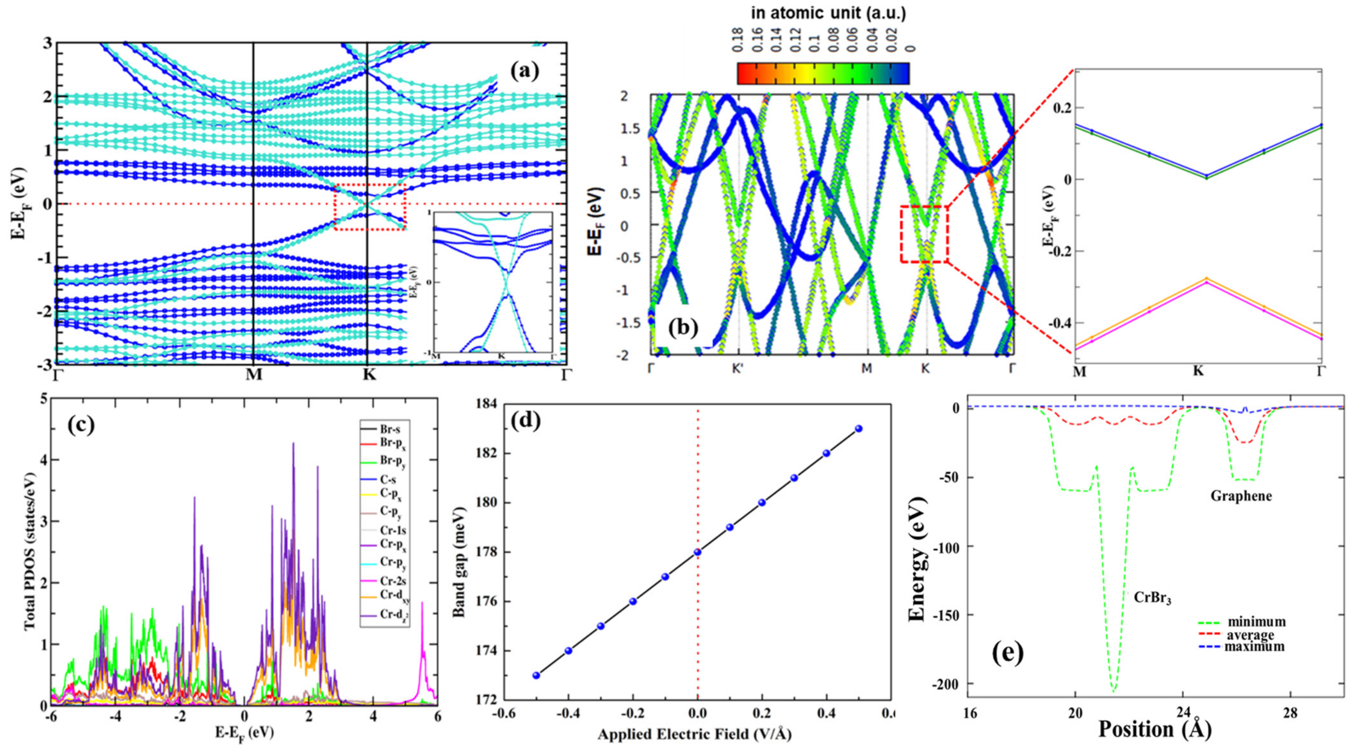

FIG. 2. (a) Spin-polarized electronic band structure calculation of Gr-CrBr$_3$ heterostructure in absence of spin-orbit coupling (SOC). The blue and cyan line depicts spin-up and spin-down states, respectively. Inset shows the zoomed-in image of the Dirac cone near the Fermi level. (b) Projected band structure of Gr-CrBr$_3$ heterostructure with the implementation of relativistic effects. Zoomed image shows the splitting of energy level and gapped state at K point. The color bar represents the magnitude of projection (scale in atomic units). (c) Projected density of states (PDoS) calculation of the Gr-CrBr$_3$ heterostructure in the presence of SOC. (d) Modulation of the band gap with respect to the external applied electric field effect in the heterostructure. (e) DFT simulated local potential distribution of the Gr-CrBr$_3$ heterostructure with a contribution from both CrBr$_3$ monolayer and graphene sheet along z direction.

due to the proximity effect between graphene and ferromagnetic, CrBr$_3$. It is obvious that Cr d orbitals will have more intense peak because of presence of intrinsic magnetic character. Therefore stemming graphene on ferromagnetic CrBr$_3$ exerts staggered potential at a distinct interplanar spacing giving rise to hybridization, charge rearrangement, and induce magnetism via proximity integration.

Along with the relativistic effect and proximity coupling, vdW heterostructures also exhibit unique features on modulating electronic nature via externally applying electric field in Gr-CrBr$_3$ heterostructure. We explore the effect of applied electric field in tuning global band gap (shown in Appendix Figs. 5 and 6) of Gr-CrBr$_3$ heterobilayer system. The band gap reduces, i.e., tending to close with decreasing strength of electric field towards the reverse (negative) bias as shown in Fig. 2(d). The modulating trend of band gap is found to be linear with the increasing strength of electric field. This indicates combination of electric field and SOC to be a convincing strategy to modulate electronic behavior of Gr-CrBr$_3$ heterostructure. The band gap of heterobilayer systems is found to be open as sufficient electric field is applied as shown in Appendix Fig. 5(a). When the strength of electric field is increased to 0.5 V/Å, the band gap reaches around 183 meV, which is higher than that of 0 V/Å. When forward bias is applied in c direction of the heterostructure, redistribution of charge will leverage Rashba SOC extrinsically in Gr-CrBr$_3$ heterolayer and it has the possibility of breaking inversion symmetry. The inversion symmetry breaking can be realized using local potential distribution at both layers as described in Fig. 2(e). The uneven distribution of electronic states over heterointerface gives rise to nonzero surface charge and subsequent electrostatic potential due to accumulation of local potential energy [shown in Fig. 2(e)]. The evenly distributed delocalization is clearly evident from local potential energy profile. The charge neutrality is noticed at interface due to presence of proximity interaction. This evenly distribution confirms average energy values at zero level with respect to various locations over the interface, indicating complete charge neutrality and inversion symmetry breaking. These combined analyses of band gap modulation and local potential energy profile shows delocalization of electronic states over the proximitized heterointerface.

To identify topologically nontrivial phase, we have calculated Berry curvatures and evolution of WCC for Gr-CrBr$_3$ heterostructure. We evaluate Berry curvature by integrating over K or K' symmetry point and can acquire Chern number for each valley from tight-binding Hamiltonian. It is seen from Fig. 1(b), each valleys take similar topological charge $C_K = -C_{K'} = 1$ due to staggered AB sublattice potential. As the topological charge for valleys are similar, the total Chern number is vanishing $C_K + C_{K'} = 0$. By subtracting the Chern number values for each valley K and K' contributes to the QVH phase with $C_v = (C_K - C_{K'})/2 = 1$. Since, the global band gap near K point does not close even in absence of

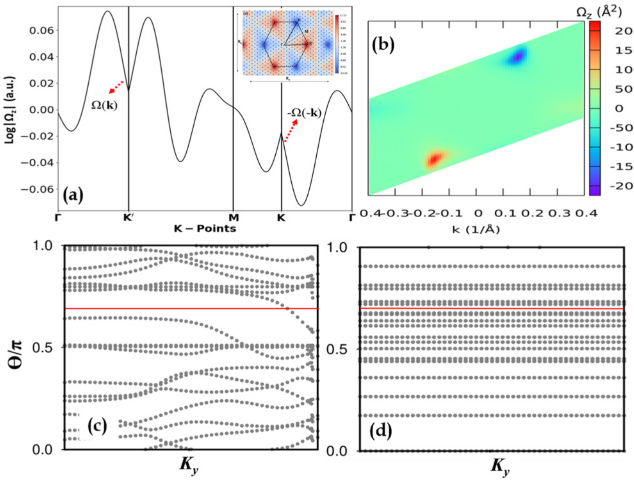

FIG. 3. (a) Calculated Berry curvature of Gr-CrBr$_3$ heterostructure along high-symmetry points. The red dashed arrow shows $\Omega(k)$ and $-\Omega(-k)$ (in a logarithmic scale). The inset shows Berry curvature in 2D k plane. (b) Density plots of Berry curvature for the occupied band for the first Brillouin zone of Gr-CrBr$_3$ heterostructure. (c) Evolution of Wannier charge center (WCC) for Gr-CrBr$_3$ bilayer system in the presence of SOC (d) in absence of SOC. The red solid line is a reference line. Odd number times the reference line is crossed by the evolution line indicating the system to be topologically nontrivial.

electric field, final value of valley Chern number remains invariant as $C_v = 1$. Therefore such behavior is considered to have QAH phase exhibiting valley contrasting effect. Figure 3(a) shows the calculated Berry curvature $\Omega(k)$ summed over all occupied bands along high-symmetry points in first Brillouin zone as shown in Eq. (A3) in Appendix. The inset in Figure 3(a) shows Berry curvature distribution over 2D K plane, where the Fermi level has already been shifted into the heterostructure band gap region. It is seen that the Berry curvature is sizable and takes opposite signs in the vicinity of K and K' valleys revealing valley contrasting characteristic. The Berry curvatures are primarily localized near high-symmetry points K and K'. The density of Berry curvature at valley K is slightly different from valley K', resulting in the inequality of Chern number obtained by valley K and K'. The Berry curvature is invariant under spatial inversion, which transforms K and K' into each other. Therefore breaking of inversion and time reversal symmetry is the prime factor for realizing valley contrasting behavior. The nonvanishing valley Chern number indicates opening of band gap to be topologically nontrivial, signifying the presence of QVH effect in heterostructure system. The nontrivial global band gap is found to be 178 meV, much larger than that of the reported QAH systems [5,43]. This amplified SOC in graphene arises due to the proximity coupling with ferromagnetic CrBr$_3$, breaking inversion symmetry of graphene plane, and leads to strong Rashba SOC.

Figure 3(b) describes density plots of the Berry curvature for the Gr-CrBr$_3$ heterostructure system. The Brillouin zone is parameterized over momentum space of heterostructure system. The Berry curvature exhibit both positive and negative values at valleys K and K' corroborating with Fig. 3(a) for realizing valley contrasting phenomena. It is clearly evident from Fig. 3(a), the valley is inverted and peaked at valley K' and K, respectively. The inverted and peaked valley can be correlated with blue and red color in density plot of the Berry curvature [as shown in Fig. 3(b)]. The blue color depicting the Berry curvature around K' valley is divergent and red color depicts K valley to be convergent, which primarily acts like a source and a sink of the Berry curvature. This is also quite evident from the spin configuration plot as shown in Appendix Fig. 7. In this regard, the Berry curvature will give rise to an anomalous transverse velocity for Bloch electrons under an in-plane longitudinal electric field [44]. Thus charge carriers in K and K' valley transmit in the opposite direction realizing valley contrasting nature and giving rise to the QVH effect. Figure 3(c) displays the evolution of WCC with respect to momentum space in the Gr-CrBr$_3$ bilayer system as described in Eq. (A6) of Appendix. The evolution of WCC in momentum space is calculated by considering U(2N) non-Abelian Berry connection [45]. To show topological property via evolution of WCC, we implemented a tight-binding model [46] for better visualization of topologically nontrivial states. It is clearly evident that only once the evolution line crosses red solid reference line with implementation of relativistic effect in a heterostructure system, indicating the system to be topologically nontrivial. No crossing of the evolution line through the reference line is observed leading to a topologically trivial state in the absence of SOC as shown in Fig. 3(d). Therefore odd winding number of WCC clearly signify valley contrasting phenomena and the topologically nontrivial state in the Gr-CrBr$_3$ vdW heterostructure.

Figure 4(a) illustrates the Hall coefficient in the Gr-CrBr$_3$ heterostructure as a function of a chemical potential at different temperature. Gr-CrBr$_3$ heterostructure systems show a shifting near the Fermi level (E_F) towards positive chemical potential, which signifies active participation of n-type carrier concentration. Moreover, shifting of the peak towards n-type carrier concentration attributes due to magnetic proximity coupling between graphene and ferromagnetic CrBr$_3$. There is a slight decrease in the value of the Hall coefficient in the context of temperature differing from 100 to 300 K, which can be neglected. As a consequence of valley contrasting nature obtained from Berry curvature, an anomalous Hall conductivity is observed in heterostructure systems. The nature of the anomalous Hall effect (AHE) is explained by the Berry phase of Bloch electron, which is induced by relativistic implications in the presence of magnetization due to the proximity effect modelled by complex transfer integrals [47]. In Fig. 4(b), we obtain calculated σ_{xy} as a function of energy. The extreme maxima of the valley K and K' is denoted by red dot-dashed line signifying presence of valley localized quantum Hall effect. The anomalous Hall conductivity (AHC) is obtained intrinsically in the absence of external electric field because of nonzero surface charge and delocalized electrostatic potential created at heterointerface via magnetic proximity coupling. The plateau near zero energy in AHC hints us possibility of possessing quantization of Landau levels due to the presence of binary degrees of freedom resulting valley contrasting QAH effect. However, a small plateau near zero energy also signifies the existence of Hall conductivity in the limit of low concentration intrinsically due to magnetic proximity interaction. The inset

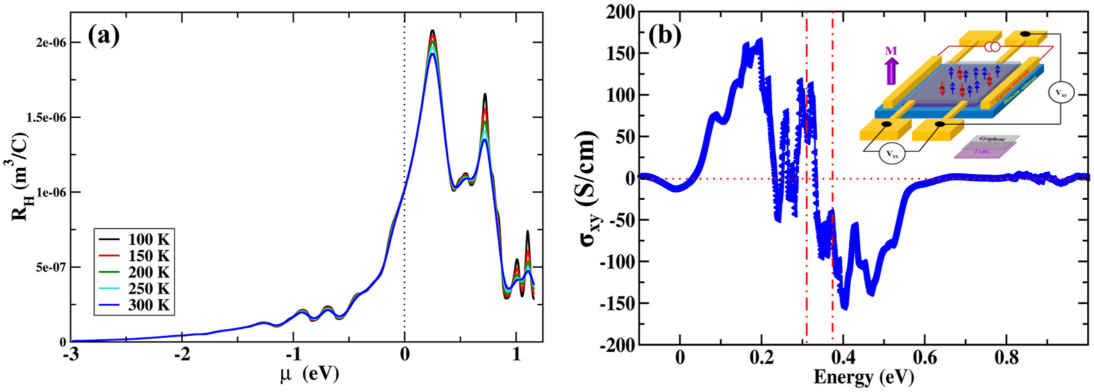

FIG. 4. (a) Calculation of the Hall coefficient in the Gr-$CrBr_3$ heterostructure with respect to the chemical potential at different temperature. (b) The calculated anomalous Hall conductivity as a function of energy. The two dot-dashed lines depict the two valleys. Inset displays scheme of QVH effect in the vdW heterostructure of graphene on monolayer $CrBr_3$.

in Fig. 4(b) depicts a schematic model of a QVH device connected with a current electrode for applying the bias current in Gr-$CrBr_3$ heterostructure system for measuring Hall resistance. The presence of SOC and proximity coupling of ferromagnetic $CrBr_3$ with graphene leads in breaking of time reversal symmetry for realizing the QVH effect. However, alongside proximity coupling and SOC the QVH phase also occurs with application of bias current, which modifies the carrier density close to zero. Moreover, the domains of magnetic material strongly interacts with applied bias current, which electrically tunes polarization of magnetic domains [41]. The Hall resistance can also be driven by proximity coupling with ferromagnetic $CrBr_3$. We leverage this flexibility in our device prototype. Modelling of such a device prototype can be introduced in any platform for experimental realization of the QVH effect.

IV. CONCLUSION

In conclusion, we systematically investigate magnetic proximity induced quantum valley Hall (QVH) effect in Gr-$CrBr_3$ heterostructures based on *ab initio* DFT simulations, WANNIER90 package and WANNIERTOOL. The global band gap of 178 meV is opened near high-symmetry point at Fermi region with implications of relativistic effect, which can be easily modulated with external electric field or incorporation of staggered AB sublattice potential. This intrinsically breaks inversion symmetry of graphene bipartite sublattice leading to strong Rashba SOC. In addition to SOC and magnetism, an external electric field helps to modulate electronic properties of heterobilayer system. The calculated Berry curvature indicates that system can represent characteristics of the valley contrasting the QAH effect. The valley contrasting nature is also evident from a nonzero value of two extreme valleys peaked at K' and K, typically behaved like a source and sink of Berry curvature. The odd winding number (valley Chern number $C_v = 1$) associated from WCC clearly signifies breaking of time reversal symmetry, possessing a topologically nontrivial state. The AHC is obtained in the absence of an external electric field due to nonzero surface charge and local potential originated at the interface via magnetic proximity coupling. The calculated value of the Hall coefficient in the heterostructure system is found to be shifted towards right (positive chemical potential) due to the magnetic proximity coupling between graphene and ferromagnetic $CrBr_3$. Therefore the Gr-$CrBr_3$ heterostructure systems provide a promising platform to detect valley contrasting QAH Effect. This finding will engulf the new approach in realizing experimental implications in unveiling possible vdW systems for the QVH effect.

ACKNOWLEDGMENTS

M.B. and P.D. thank IIT, Kharagpur, and Tezpur University for providing High performing cluster computing (HPCC) facility. P.D. acknowledge NBIOs award project, Department of Biotechnology, Government of India, vide Grant No. 102/IFD/SAN/5142/2018-19. M.B. would like to acknowledge Department of Science and Technology, Government of India for providing INSPIRE fellowship. S.K.B. acknowledges NISER and MRC, IISc. Parts of calculations with licensed VASP software are also performed in the KALINGA and NISERDFT High Performance Computing Facility, NISER and Cluster facility of SERC, IISc.

APPENDIX

1. Berry curvature and Wannier charge center

In this Appendix, we explain details about the Berry curvature and WCC use to determine topologically nontrivial nature in proximitized Gr-$CrBr_3$ heterostructure systems. The Berry curvature is associated with the Berry connection. Considering the wave function $|\psi(R)\rangle$ for mth eigenstate of Hamiltonian $H(R)$, where R is parametrized $R = (R_1, R_2,..., R_m)$. The two overlapping wave functions microscopically differentiated by ΔR in the parameter space is written as [48]

$$\begin{aligned}\langle\psi(R)|\psi(R+\Delta R)\rangle &= 1 + \Delta R\langle\psi(R)|\nabla_R\psi(R)\rangle\\ &= \exp(-i\Delta RA_M(R)).\end{aligned} \quad (A1)$$

Here, $\mathrm{A}_M(R) = \mathrm{i}\langle\psi(R)|\nabla_R\psi(R)\rangle$ represents the Berry connection. It contemplates as a vector potential and the curl $\Omega_M = \nabla_R \times \mathrm{A}_M(R)$, named as the Berry curvature, which acts like a magnetic field in the parameter space R. By using the gauge transformation between the Bloch electron and real-space Wannier functions, the Berry curvature is evaluated as [49]

$$\Omega(k) = \sum_m f_m \Omega_m(k), \tag{A2}$$

$$\Omega_m(k) = -2Im \sum_{n \neq m} \frac{\langle \psi_{mk} | v_x | \psi_{nk} \rangle \langle \psi_{nk} | v_y | \psi_{mk} \rangle}{(E_n - E_m)^2}. \tag{A3}$$

Here, summation is over all occupied states in momentum space, E_m is an eigenvalue of the Bloch electron wave functions $|\psi_{mk}\rangle$, f_m denotes the Fermi-Dirac distribution functions, v_x and v_y are the velocity operators. Moreover, the Chern number can be calculated by integrating Berry curvature over the first Brillouin zone. Another alternative way to calculate Chern topological invariant is by evaluating WCC. The correlation of Wannier functions to topology is linked by the matrix element of the position operator in the Wannier basis to the Berry connection. The formulation of charge center as well as the spread can be written in terms of Bloch wave functions $|\psi_{mk}\rangle$ [50],

$$\bar{r}_n = \frac{V}{(2\pi)^3} \int d^3k \langle \psi_{mk} | \nabla_k | \psi_{mk} \rangle. \tag{A4}$$

The wave function of Bloch electron is associated with the Wannier functions having a gauge freedom.

The idea of using WCC is to evaluate topological invariance and the expression of charge centers in Eq. (A4) is proportional to the Berry curvature. The topological invariant is determined by calculating WCC in 2D k plane for occupied bands. The projection operator for occupied bands is written as

$$\hat{P}_{ky} = \sum_{m \epsilon 0, k_x} |\psi_{mk}\rangle\langle\psi_{mk}|. \tag{A5}$$

Here, 0 is the summation denotes the occupied bands.

The eigenvalue is considered here for the projected position operator written as

$$\hat{X}_p(k_y) = \hat{P}_{ky} \hat{X} \hat{P}_{ky} = C_v. \tag{A6}$$

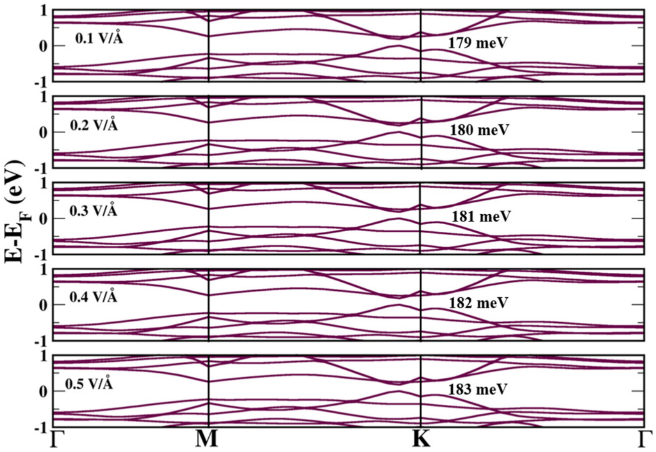

FIG. 5. Modulation of band topology with the application of perpendicular electric field in positive Z direction from 0.1 to 0.5 V/Å in Gr-CrBr$_3$ bilayer systems.

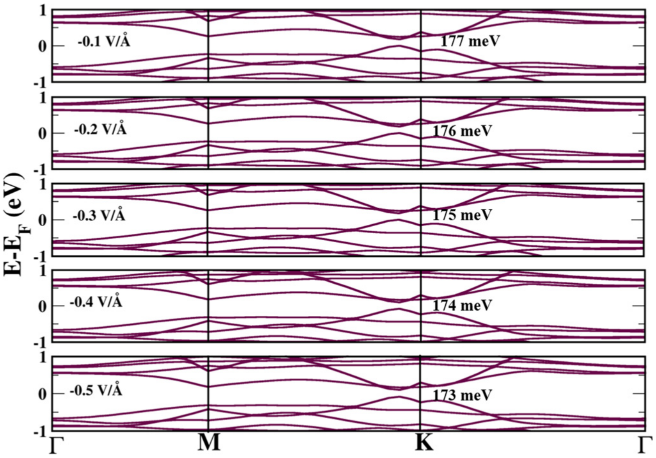

FIG. 6. Modulation of electronic band structure with the application of perpendicular electric field in negative Z direction from −0.1 to −0.5 V/Å in the Gr-CrBr$_3$ bilayer system.

Here, C_v corresponds to the valley Chern number, describing topological invariance in system.

For 2D system, we consider k and t as two independent coordinates, the Berry curvature will be the difference between the derivation with respect to t keeping k constant and derivation with respect to k keeping t constant. The integration of the Berry curvature over full Brillouin zone and difference in the projection operator will provide the total Chern number of a 2D system.

By obtaining the Chern number from the evolution of WCC and Berry curvature, the anomalous Hall conductivity is obtained by $\sigma_{xy}= e^2/h$ C. The Chern number provides the information about the number of dissipationless transport channel present in the Gr-CrBr$_3$ vdW heterostructure.

2. Electric field mediated band topology

Figure 5 depicts modulation of the electronic band structure with the variation in applied electric field in forward bias (+Z direction) from 0.1 to 0.5 V/Å in the Gr-CrBr$_3$ heterostructure system. It displays the opening of global band

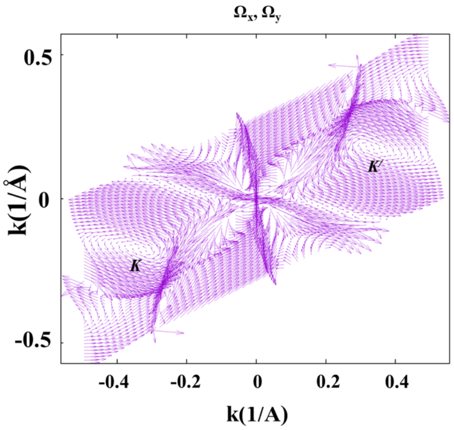

FIG. 7. Spin configuration in the momentum space around K and K' for Gr-CrBr$_3$ bilayer system.

gap from 179 to 183 meV at the high-symmetry point near the Fermi region (E_F).

Here, Fig. 6 shows the modulation of band topology with the variation in applied electric field in reverse bias ($-Z$ direction) from -0.1 to -0.5 V/Å in the Gr-CrBr$_3$ heterostructure system. It displays the closing of global band gap from 177 to 173 meV at the high-symmetry point near the Fermi region (E_F).

3. Normalized Berry curvature

By plotting spin configuration in Fig. 7 by normalizing the Berry curvature around K_x-K_y plane, we see the spin texture at K' and K to be divergent and convergent acting like a source and sink. The spin texture at K' and K are opposite to each other, correlating well with Figs. 3(a) and 3(b). This observation gives a clear insight of the valley contrasting QAH phenomena.

---

[1] M. Bora and P. Deb, J. Phys. Mater. **4**, 034014 (2021).

[2] M. Z. Hasan and C. L. Kane, Rev. Mod. Phys. **82**, 3045 (2010).

[3] X.-L. Qi, T. L. Hughes, and S.-C. Zhang, Phys. Rev. B **78**, 195424 (2008).

[4] H. Fu, C.-X. Liu, and B. Yan, Sci. Adv. **6**, eaaz0948 (2020).

[5] R. Yu, W. Zhang, H. J. Zhang, S. C. Zhang, X. Dai, and Z. Fang, Science **329**, 61 (2010).

[6] F. D. M. Haldane, Phys. Rev. Lett. **61**, 2015 (1988).

[7] C.-Z. Chang, W. Zhao, D. Y. Kim, H. Zhang, B. A. Assaf, D. Heiman, S. C. Zhang, C. Liu, M. H. W. Chan, and J. S. Moodera, Nat. Mater. **14**, 473 (2015).

[8] Y. Ou, C. Liu, G. Jiang, Y. Feng, D. Zhao, W. Wu, X.-X. Wang, W. Li, C. Song, L.-L. Wang, W. Wang, W. Wu, Y. Wang, K. He, X.-C. Ma, and Q.-K. Xue, Adv. Mater. **30**, 1703062 (2018).

[9] Z. Qiao, H. Jiang, X. Li, Y. Yao, and Q. Niu, Phys. Rev. B **85**, 115439 (2012).

[10] J. Lee, K. F. Mak, and J. Shan, Nat. Nanotechnol. **11**, 421 (2016).

[11] K. F. Mak, K. L. Mcgill, J. Park, and P. L. Mceuen, Science **344**, 1489 (2014).

[12] X. Zhai and Y. M. Blanter, Phys. Rev. B **101**, 155425 (2020).

[13] J. H. J. Martiny, K. Kaasbjerg, and A.-P. Jauho, Phys. Rev. B **100**, 155414 (2019).

[14] L. Xu, M. Yang, L. Shen, J. Zhou, T. Zhu, and Y. P. Feng, Phys. Rev. B **97**, 041405(R) (2018).

[15] T. Olsen and I. Souza, Phys. Rev. B **92**, 125146 (2015).

[16] B. T. Zhou, K. Taguchi, Y. Kawaguchi, Y. Tanaka, and K. T. Law, Commun. Phys. **2**, 26 (2019).

[17] J. H. Garcia, M. Vila, C.-H. Hsu, X. Waintal, V. M. Pereira, and S. Roche, Phys. Rev. Lett. **125**, 256603 (2020).

[18] J. O. Island, X. Cui, C. Lewandowski, J. Y. Khoo, E. M. Spanton, H. Zhou, D. Rhodes, J. C. Hone, T. Taniguchi, K. Watanabe, L. S. Levitov, M. P. Zaletel, and Y. A. F., Nature (London) **571**, 85 (2019).

[19] K. Nagata, S. Y. Matsushita, X.-C. Pan, K.-K. Huynh, and K. Tanigaki, Phys. Rev. Materials **5**, 024208 (2021).

[20] Igor Žutić, J. Fabian, and S. Sarma, Rev. Mod. Phys. **76**, 323 (2004).

[21] M. Gmitra, S. Konschuh, C. Ertler, C. Ambrosch-Draxl, and J. Fabian, Phys. Rev. B **80**, 235431 (2009).

[22] J. Ding, Z. Qiao, W. Feng, Y. Yao, and Q. Niu, Phys. Rev. B **84**, 195444 (2011).

[23] P. Högl, T. Frank, K. Zollner, D. Kochan, M. Gmitra, and J. Fabian, Phys. Rev. Lett. **124**, 136403 (2020).

[24] J. Zhang, B. Zhao, Y. Yao, and Z. Yang, Phys. Rev. B **92**, 165418 (2015).

[25] K. S. Burch, D. Mandrus, and J.-G. Park, Nature (London) **563**, 47 (2018).

[26] A. M. Alsharari, M. M. Asmar, and S. E. Ulloa, Phys. Rev. B **97**, 241104(R) (2018).

[27] E. McCann, Phys. Rev. B **74**, 161403(R) (2006).

[28] S. Bhowal and S. Satpathy, npj Comput. Mater. **5**, 61 (2019).

[29] A. K. Geim and I. V. Grigorieva, Nature (London) **499**, 419 (2013).

[30] L. Webster and J.-A. Yan, Phys. Rev. B **98**, 144411 (2018).

[31] S. K. Behera, M. Bora, C. S. S. Paul, and P. Deb, Phys. Chem. Chem. Phys. **21**, 25788 (2019).

[32] C.D. Immer, J.L. Sarrao, Z. Fisk, A. Lacerda, C. Mielke, J. D. Thompson, Phys. Rev. B **56**, 719 (1997).

[33] C. L. Kane and E. J. Mele, Phys. Rev. Lett. **95**, 146802 (2005).

[34] P. Giannozzi, S. Baroni, N. Bonini, M. Calandra, R. Car, C. Cavazzoni, D. Ceresoli, G. L. Chiarotti, M. Cococcioni, I. Dabo, A. D. Corso, S. D. Gironcoli, S. Fabris, G. Fratesi, R. Gebauer, U. Gerstmann, C. Gougoussis, A. Kokalj, M. Lazzeri, L. Martin-Samos *et al.*, J. Phys.: Condens. Matter **21**, 395502 (2009).

[35] J. P. Perdew, K. Burke, and M. Ernzerhof, Phys. Rev. Lett. **77**, 3865 (1996).

[36] A. I. Liechtenstein, V. I. Anisimov, and J. Zaanen, Phys. Rev. B **52**, R5467 (1995).

[37] J. Heyd and G. E. Scuseria, J. Chem. Phys. **118**, 8207 (2003).

[38] G. Kresse and J. Furthmuller, Phys. Rev. B **54**, 11169 (1996).

[39] S. Grimme, J. Comput. Chem. **27**, 1787 (2006).

[40] N. Marzari, A. A. Mostofi, J. R. Yates, I. Souza, and D. Vanderbilt, Rev. Mod. Phys. **84**, 1419 (2012).

[41] Q. Wu, S. Zhang, H.-F. Song, M. Troyer, and A. A. Soluyanov, Comput. Phys. Commun. **224**, 405 (2018).

[42] G. Giovannetti, P. A. Khomyakov, G. Brocks, P. J. Kelly, and J. van den Brink, Phys. Rev. B **76**, 073103 (2007).

[43] Q.-Z. Wang, X. Liu, H.-J. Zhang, N. Samarth, S.-C. Zhang, and C.-X. Liu, Phys. Rev. Lett. **113**, 147201 (2014).

[44] D. Xiao, M.-C. Chang, and Q. Niu, Rev. Mod. Phys. **82**, 1959 (2010).

[45] A. A. Soluyanov and D. Vanderbilt, Phys. Rev. B **83**, 235401 (2011).

[46] S. Schulz and G. Czycholl, Phys. Rev. B **72**, 165317 (2005).

[47] M. Onoda and N. Nagaosa, J. Phys. Soc. Jpn. **71**, 19 (2002).

[48] Hongming Weng, Y. Rui, H. Xiao, D. Xi, and F. Zhong, Adv. Phys. **64**, 227 (2015).

[49] X. Wang, J. R. Yates, I. Souza, and D. Vanderbilt, Phys. Rev. B **74**, 195118 (2006).

[50] N. Marzari and D. Vanderbilt, Phys. Rev. B **56**, 12847 (1997).